



Electrodeposition of Ni nanoparticles from deep eutectic solvent and aqueous solution promoting high stability electrocatalyst for hydrogen and oxygen evolution reactions

Safya Elsharkawya^{1,2} · Sherin Hammad^{1,2} · Ibrahim El-hallaga^{1,2}

Received: 4 February 2022 / Revised: 19 April 2022 / Accepted: 20 April 2022 / Published online: 17 May 2022
© The Author(s) 2022

Abstract

Nanostructured Ni films were synthesized from two distinct baths and were assessed as electrocatalysts for hydrogen evolution reaction (HER) and oxygen evolution reaction (OER) in 1 M KOH. Herein, Ni was electrodeposited from two separate solvents, the aqueous acetate buffer and ethaline solvent as a kind of deep eutectic solvents (DESS), and both the deposited films were investigated as electrocatalysts for HER and OER. The electrodeposition parameters such as pH and deposition potential were studied. The electrodeposition process was performed using chronoamperometry technique and Ni deposits were characterized by scanning electron microscopy (SEM), transmission electron microscopy (TEM), energy-dispersive X-ray spectroscopy (EDX), and X-ray diffraction (XRD). Fabricated Ni@PGE deposit from ethaline only requires an overpotential of -154 mV and 350 mV to achieve a current density of 10 mA cm^{-2} for HER and OER, respectively. While, Ni@PGE from acetate requires an overpotential of -164 mV and 400 mV to produce the current density of 10 mA cm^{-2} for HER and OER.

Keywords Ni electrodeposition · Deep eutectic solvents · Hydrogen evolution reaction · Oxygen evolution reaction · Acetate bath

Introduction

Excessive usage of fossil fuel-based energy systems (such as coal, petroleum, and natural gas) pollutes the environment. As a result, the globe invests heavily in the development of renewable and green energy applications [1–8]. Because of its high energy density (140 MJ kg^{-1}) and zero emissions, hydrogen is one of the most promising energy sources [9–12]. Thus, electrochemical water splitting in an alkaline medium is a facile and effective approach for producing pure hydrogen and oxygen with no pollution [13–16]. However, both the hydrogen evolution reaction

(HER) and the oxygen evolution reaction (OER) have very slow kinetics and require a high overpotential to happen [17–20]. As a result, the development of an intrinsic electrocatalyst with high electrocatalytic activity is critical. To date, the most suited electrocatalysts that have been used for HER are Pt and Ru, or Ir oxides for OER [21–24]. Nevertheless, the insufficiency and high cost of these metals prevent their applications [25, 26]. To overcome these challenges, the design of an electrocatalyst with a high activity towards HER and OER is important and urgent. Thus, there are many strategies employed to design an electrocatalyst and develop its surface electronic structure with more active sites to enhance its catalytic performance. So, the challenge is based on discovering a non-precious catalyst with high catalytic activity and stability to be available for both HER and OER. Among transition metals, Ni was selected as it has good electrocatalytic activity towards HER and OER. Ni has remarkable properties which make it a terrific catalyst used in different related energy applications such as supercapacitors, hydrogen evolution reaction, and oxygen evolution reaction [27–30]. Y et al. have synthesized $\alpha(\text{Ni}(\text{OH})_2)$ nanoplates supported on Pt by hydrothermal

✉ Safya Elsharkawya
safya.elsharkawy@science.tanta.edu.eg

✉ Ibrahim El-hallaga
ibrahim.elhallag@yahoo.com

¹ Faculty of Science, Chemistry Department, Tanta University, Tanta, Egypt

² Faculty of Pharmacy, Analytical Chemistry Department, Tanta University, Tanta, Egypt

method with high activity towards HER [31]. $\alpha(\text{Ni}(\text{OH})_2)/\text{NF}$ was prepared via electrochemical deposition by Balarm et al. introducing high activity for OER. Rao et al. have designed hexagonal $\text{Ni}(\text{OH})_2$ supported on NF via hydrothermal preparation which produces an overpotential of 172 mV for HER to reach a current density of 20 mA cm^{-2} and 330 mV to reach a current density of 50 mA cm^{-2} for OER in 1 M KOH [32]. Taşçi et al. have constructed 3D Ni nanodomains via physical vapor deposition which possesses low overpotential of 85 mV and high stability for HER [33]. $\text{Ni}(\text{OH})_2/\text{Ni}/\text{CC}$ electrode introduces 458 mV value of overpotential to give 100 mA cm^{-2} for OER [34]. Most of the catalysts that are used for water splitting are in a powder form and need a binder or adhesive agent to attach to the electrode surface as Nafion and PTFE which blocks the active sites of the catalyst during the time, decreasing its stability and its catalytic activity. The electrodeposition technique is one of the most important and cheap methods that is used for nanomaterial preparation which assists the catalyst preparation with high activity. Therefore, in this work, we improved the properties of the Ni catalyst producing high catalytic activity for both HER and OER depending on a simple and cheap method via the electrodeposition technique. The bath composition and pH affect the deposit morphology, coating properties, and adhesion. First, we prepared two different electrolytes with different properties and made the deposition process of Ni from them. The first electrolyte is acetate buffer and the second is deep eutectic solvent (DES) which has unique physical and chemical properties [35]. DESs have distinct properties as they have wide potential window. Thus, many metals and their alloys which are difficult to be fabricated from the aqueous solvents because of the passivation of the electrode are easily electrodeposited from DESs. Moreover, an increase in the temperature of DESs produces narrower electrochemical windows and in larger capacitance currents [36]. The most popular one is ethaline which consists of choline chloride and ethylene glycol. It is prepared by mixing them with a different new ratio 1:3 until forming a homogenous colorless solution. The two different electrolytes give us two different properties, and morphologies for Ni deposits. Second, we evaluated the catalytic activity, the kinetics, and the efficiency of the fabricated electrodes from the two solvents for HER and OER.

Experimental

Chemicals

All chemicals are purchased from Sigma and Aldrich without further purification. We made two baths, one in an aqueous solution and the other in ethaline. Table 1 contains all

Table 1 Chemicals used and their chemical formula

Chemical compound	Chemical formula	Purity
Acetic acid	CH_3COOH	98%
Sodium acetate	CH_3COONa	98%
Choline chloride (ChCl)	$\text{HOC}_2\text{H}_4\text{N}(\text{CH}_3)_3\text{Cl}$	99%
Ethylene glycol (EG)	$\text{C}_2\text{H}_6\text{O}_2$	99%
Nickel chloride	$\text{NiCl}_2 \cdot 6\text{H}_2\text{O}$	99%
Potassium hydroxide	KOH	99%

the chemicals that are used and their chemical formula with their purity.

Fabrication of Ni nanostructures from DES bath

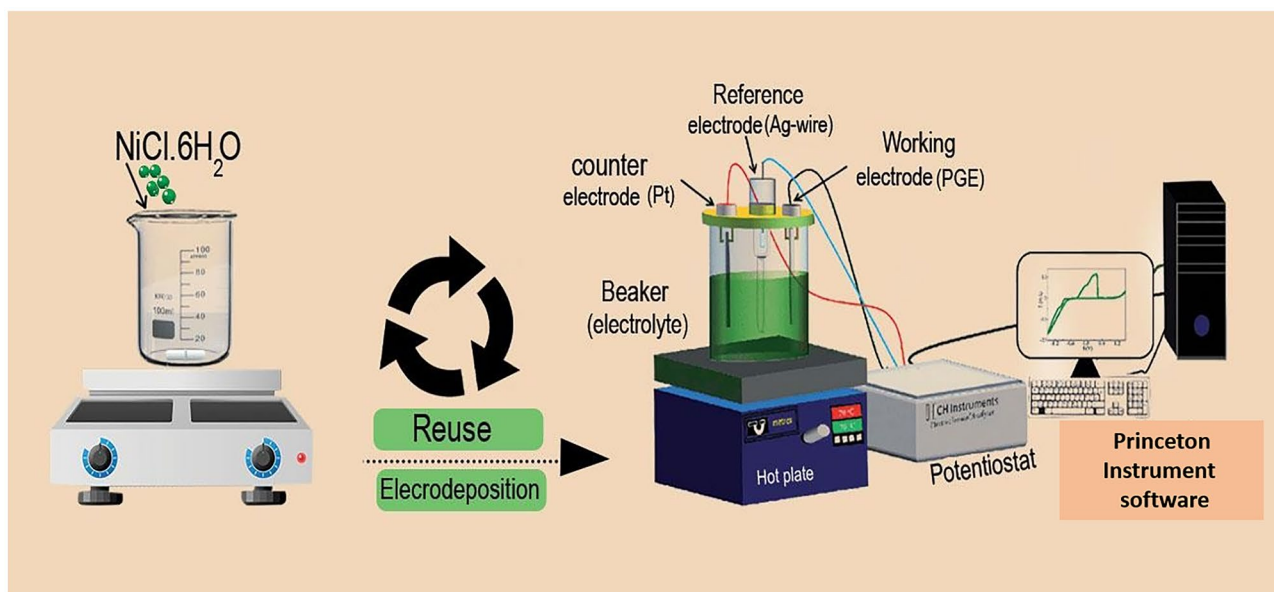
DES was developed with a 1:3 molar ratio of choline chloride (ChCl) and ethylene glycol (EG) (this solvent is known as ethaline). It was prepared by mixing the molar ratio at temperature 333 K until a colorless liquid solvent was formed. Afterward, 0.4 M of $\text{NiCl}_2 \cdot 6\text{H}_2\text{O}$ was added to ethaline. The electrodeposition process and electrochemical measurements were carried out on an electrochemical work station via a computer-controlled potentiostat/galvanostat model 273 A from Princeton Applied Research, Oak Ridge, TN, the USA, with software of 270/250-PAR 10-mL glass cell containing three electrodes: Pencil graphite electrode (PGE) with 0.0314 cm^2 surface area was employed as a working electrode, a silver wire was used as a quasi-reference electrode (QRE), and a platinum wire was used as the counter electrode. The utilization of this type of quasi-reference electrode prevents the possible impurities from the working electrode [37–39]. The working electrode was cleaned and smoothed before each run by adding in conc. HCl for 1 min to remove any attached particles or contaminations to the surface. After that, polishing was done with emery papers having different grades (from 1200 to 2500 P). The electrodeposition process was performed at a constant potential of -0.98 V under mild stirring at 318 K for 900 s. Scheme 1 illustrates the deposition process from DES.

Fabrication of Ni nanostructures from acetate bath

In this section, the electrolyte of 0.4 M $\text{NiCl}_2 \cdot 6\text{H}_2\text{O}$ was made in a pH 5.8 acetate buffer (0.2 M) calibrated by 0.1 M NaOH. The deposition process was performed at a potential of -1.1 V for 900 s at room temperature with slight agitation by the same previous electrodes.

Material characterization

Scanning electron microscopy (SEM) was used to exhibit the morphology of the deposited materials.



Scheme 1 The electrodeposition of Ni nanoparticles from ethaline solvent is depicted schematically

Energy-dispersive X-ray spectroscopy (EDX) was used to investigate the composition of the deposits: SEM instrument (JEOL, JSM IT-100) with a maximum magnification of $300,000\times$, maximum resolution of 3 nm, and maximum acceleration voltage of 30 kV; EDX instrument (silicon drift detector) with an energy resolution about 129 eV or better analysis condition of WD 10 mm and voltage 20 kV. Transmission electron microscopy (TEM) was used to investigate the internal structure of the deposited Ni from DES: TEM instrument (JEOL, JEM-200) with a maximum magnification of 1.5 million \times . X-ray diffraction (XRD) was used to show the crystallography structure of the deposited electrocatalysts: XRD instrument (Shimadzu XRD 6000, X-ray diffractometer Cu k alpha radiation (wavelength = 1.5418 \AA)). Both films of Ni thickness were very small, so the SEM, XRD, and EDX measurements were accomplished on the deposited films at PGE

per se to prevent the distortion of the morphology or the structure, while TEM measurement needs the material in a powder form to make a suspension solution. Therefore, the deposits were scratched carefully.

Electrochemical studies

In a conventional three-electrode electrochemical cell, the electrochemical performance of both electrodeposited Ni from acetate and ethaline was investigated. The working electrode was made up of Ni plated films, while the reference and counter electrodes were made up of Ag/AgCl (3 M KCl) and Pt wire, respectively. In the case of HER and OER measurements, linear sweep voltammetry (LSV) was used in a solution containing 1 M KOH at a scan rate of 50 mV s^{-1} at room temperature. For the fabricated Ni

Fig. 1 Cyclic voltammogram of **a** PGE in acetate solution and ethaline solvent at a scan rate of 20 mV s^{-1} at room temperature and **b** 0.4 M Ni^{2+} in acetate buffer at pH 5.8 and a scan rate of 20 mV s^{-1} at room temperature and in ethaline at a scan rate of 20 mV s^{-1} at temperature 318 K

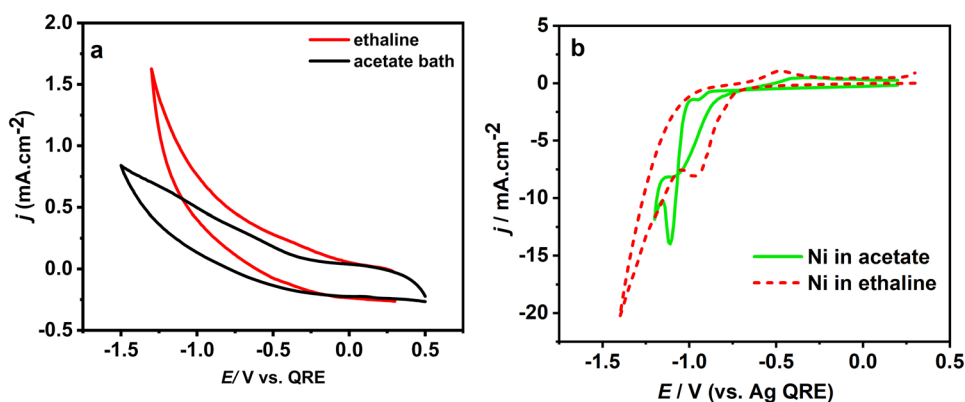
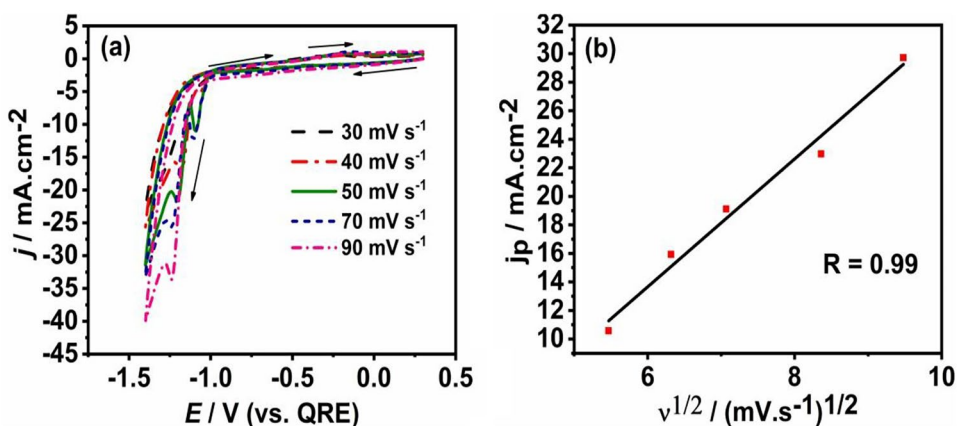


Fig. 2 **a** Cyclic voltammograms of 0.4 M $\text{NiCl}_2 \cdot 6\text{H}_2\text{O}$ at various scan rates in acetate buffer at pH 5.8 at room temperature. **b** The dependence of the cathodic peak current density (j_p) on the square root of the scan rate ($\nu^{1/2}$)



electrodes, all potential data or overpotential was related to RHE, which can be calculated using the following equation (Eq. 1) [40].

$$E_{vs\ RHE} = E_{vs\ Ag/AgCl\ (3\ M\ KCl)} + E_0\ vs\ Ag/AgCl\ (3\ M\ KCl) + 0.059 \times pH\ (E_0\ vs\ Ag/AgCl\ (3\ M\ KCl) = 0.210\ V) \quad (1)$$

where $E_{vs\ Ag/AgCl\ (3\ M\ KCl)}$ is the measured potential for HER or OER in the experiment and $E_0\ vs\ Ag/AgCl\ (3\ M\ KCl)$ is the standard electrode potential.

Results and discussion

Electrochemical fabrication of Ni nanostructures at pencil graphite electrode

Cyclic voltammetry study

To determine the appropriate electrodeposition potential, a cyclic voltammogram of 0.4 M Ni^{2+} in the aqueous acetate buffer at pH 5.8 was implemented at a scan rate of $20\ \text{mV s}^{-1}$. The control cyclic voltammetry experiment for PGE in acetate bath and ethaline was accomplished at

a scan rate of $20\ \text{mV s}^{-1}$. As presented in Fig. 1a, no peaks appeared for both the acetate solution and ethaline solvent. The cyclic voltammogram of Ni in acetate buffer is shown in Fig. 1b. Two reduction peaks exist in the reduction area, one at $-0.9\ \text{V}$ with low current density and the other at $-1.1\ \text{V}$ with a high current density, which are used for the deposition process by the CA technique, and an anodic peak at $-0.4\ \text{V}$ with tiny current density. The cyclic voltammogram of 0.4 M Ni^{2+} in ethaline at a scan rate of $20\ \text{mV s}^{-1}$ and a temperature of 318 K is shown in Fig. 1b. It is noticed that there are two redox couples observed: the oxidation peak is at $-0.55\ \text{V}$, while the reduction peak is located at $-0.98\ \text{V}$ which is used for the deposition process. It is remarkable that the reduction peak position of Ni^{2+} in ethaline is shifted to a less negative potential value as the ethaline solvent acted as a complexing agent. In the cathodic direction of the CV, a layer of HBD molecules adheres to the electrode surface, while choline chloride cations are in contact with the electrolyte forming Ni-complex which decreases the reduction potential and the nucleation process, providing smaller particle size compared to the deposited Ni from acetate. [36].

Fig. 3 **a** Cyclic voltammograms of 0.4 M $\text{NiCl}_2 \cdot 6\text{H}_2\text{O}$ in ethaline at different scan rates at 318 K. **b** The dependence of the cathodic peak current density (j_p) on the square root of the scan rate ($\nu^{1/2}$)

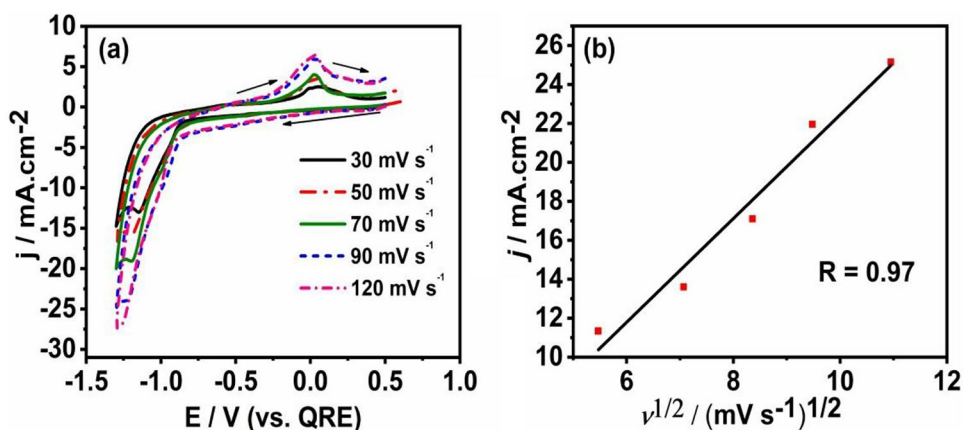
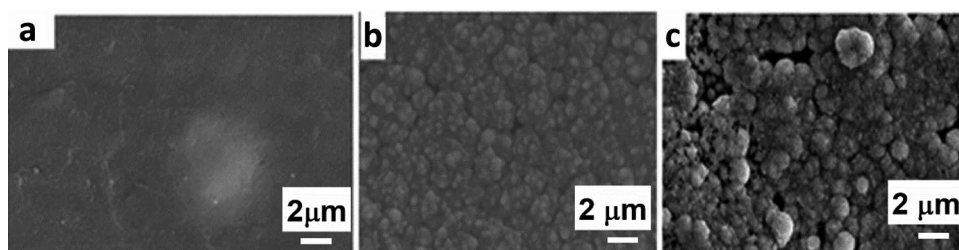


Fig. 4 SEM images of **a** bar electrode and **b** Ni deposit at PGE electrode from acetate buffer with pH 5.8 at a deposition potential of -1.1 V for 900 s. **c** Ni deposit at PGE electrode from ethaline at 318 K for 900 s



The effect of scan rate on the reduction process of Ni^{+2} ions in acetate buffer solution

More voltammetric experiments were established for calculating the diffusion coefficient of Ni^{+2} species. Figure 2a shows the CV of 0.4 M $\text{NiCl}_2 \cdot 6\text{H}_2\text{O}$ in acetate buffer solution with pH 5.8 at different scan rates of 30, 40, 50, 70, and 90 mV s^{-1} at room temperature. The position of the cathodic peak potential is shifted to a more negative value and the peak separation increases by increasing the scan rate. It was observed that both of the anodic peak current density and the reduction peak current density increase which indicates that the process of the reduction of Ni^{+2} ion species may be irreversible [41]. However, the value of the half cathodic peak width ($E_{\text{pc}} - E_{\text{pc}/2}$) changes with a small value by increasing the scan rate while the separation between the anodic peak potential and the cathodic peak potential ($E_{\text{pa}} - E_{\text{pc}}$) is 0.82 V at the lowest scan rate of 30 mV s^{-1} and $T = 298$ K. This behavior indicates the sluggishness of the rate of the electron transfer. This value is higher than the calculated theoretical value of the fast reversible exchange process being 2.3 RT/nF (30 mV when $n = 2$, $T = 298$ K),

confirming the slow nature of electron exchange between Ni^{+2} and the working electrode. Figure 2b demonstrates the variation between the cathodic peak current density and square root of scan rates which exhibits a good linear relationship, revealing that the electroactive Ni^{+2} ion species undergoes diffusion-controlled process. As discussed, the reduction of Ni^{+2} ions is a slow charge transfer process, so its diffusion coefficient can be calculated by using the Randles–Sevcik equation (Eq. 2) [42].

$$i_p = 0.4958nFACD^{1/2} \left(\frac{\alpha n \alpha F \nu}{RT} \right)^{1/2} \quad (2)$$

where i_p is the cathodic peak current in ampere, n is the number of electron transfer, A is the electrode surface area in cm^2 , F is the Faraday constant in $\text{C} \cdot \text{mol}^{-1}$, D is the diffusion coefficient in $\text{cm}^2 \text{s}^{-1}$ of Ni^{+2} ion species, ν is the scan rate in V s^{-1} , C is the concentration of Ni^{+2} species in mol cm^{-3} , α is the transfer coefficient, n_α is the number of electrons participating in the rate determining step, R is the gas constant, and T is the thermodynamic temperature. αn_α is determined from Eq. 3.

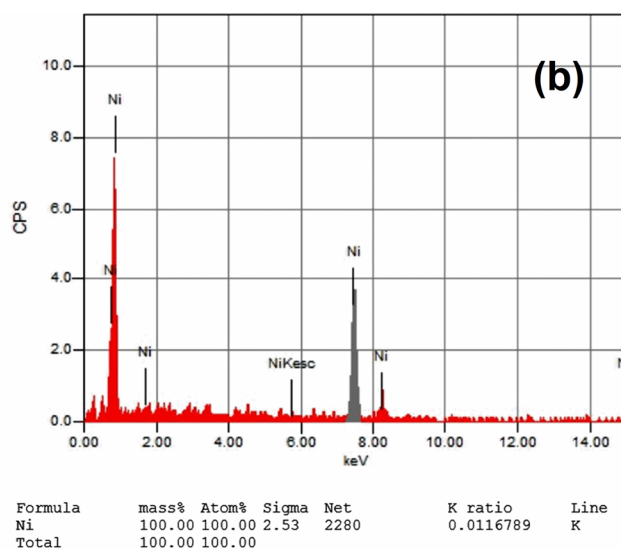
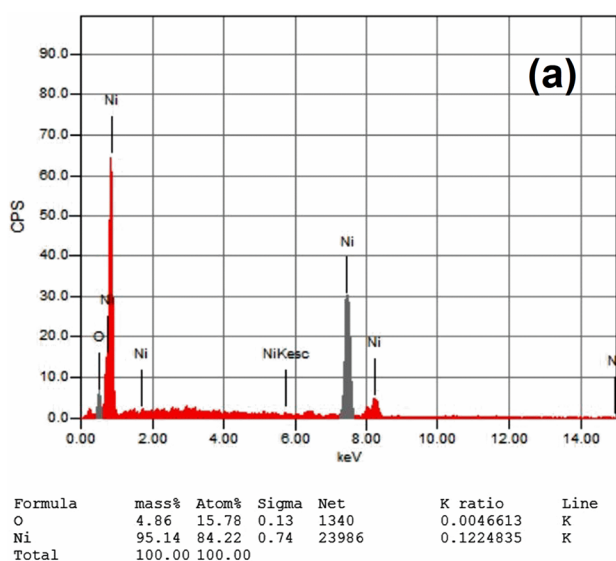


Fig. 5 EDX spectra of Ni deposits from **a** acetate and **b** ethaline

Table 2 The atomic and weight percentages of the deposited Ni nanoparticles from acetate and ethaline

	Ni peak		Oxygen peak	
	Atomic percentage	Weight percentage	Atomic percentage	Weight percentage
Ni@PGE from acetate	84.22%	95.14%	15.78%	4.86%
Ni@PGE from ethaline	100%	100%	-	-

$$\left| E_{pc} - E_{pc/2} \right| = 1.857RT / \alpha n_{\alpha} F \quad (3)$$

From this equation, the calculated value for αn_{α} equals 0.72. By substituting in Eq. 2, the calculated value for the diffusion coefficient of Ni^{+2} species is found to be $4.76 \times 10^{-7} \text{ cm}^2 \text{ s}^{-1}$.

The effect of scan rate on the reduction of Ni^{+2} ions from DES

Figure 3a represents CV measurements of 0.4 M $\text{NiCl}_2 \cdot 6\text{H}_2\text{O}$ in ethaline DES with different scan rates of 30, 50, 70, 90, and 120 mV s^{-1} at PGE at 318 K. It was found that the reduction peak potential is shifted to a more negative value and the current density for both oxidation and reduction peak increases by increasing the scan rate, providing that the nature of the electron transfer is slow. Figure 3b exhibits the variation of the peak current density with the square root of the scan rate, indicating that the electroactive species of Ni^{+2} ions undergo diffusion-controlled process, while the linear plot of Fig. 3b does not pass through the origin, which may be attributed to the nucleation and growth process that takes place during the diffusion process and/or because of the additional current that results from the resistance of the electrolyte [43–45]. Finally, the rate of charge transfer process of Ni^{+2} species is found to be a sluggish process with one-step two-electron transfer [46]. The diffusion coefficient of Ni^{+2} ions in ethaline is also calculated by using the Randles–Sevcik equation (Eq. 2) giving a value of $1.2 \times 10^{-7} \text{ cm}^2 \text{ s}^{-1}$ which is slower than the diffusion coefficient of Ni^{+2} ions in acetate buffer solution due to its higher viscosity. The peak separation (ΔE_p) for the reduction reaction of Ni^{+2} ions in the acetate bath is equal to 820 mV while in the case of Ni ions in ethaline solvent is equal to 430 mV which means that the electrode reaction of Ni^{+2} ions in the acetate buffer is slow while fast kinetics electrode reaction of Ni^{+2} ion reduction in ethaline compared with Ni^{+2} ions in the acetate according to its ΔE_p value as it has lower value.

Characterization of Ni deposits

Morphology and composition

The surface appearance, content, and crystallographic structure of Ni films produced from acetate buffer and ethaline

were investigated and characterized using SEM, TEM, EDX, and XRD. The SEM pictures and EDX for the produced Ni nanostructures from acetate buffer, ethaline, and bare PGE are presented in Fig. 4a–c.

Figure 4a exhibits the SEM image of the PGE surface before Ni electrodeposition, which reveals that the surface is empty, smooth, and featureless due to polishing scratches. The SEM image of the Ni deposit from the acetate solution, shown in Fig. 4b, indicates a homogeneous cauliflower morphology filling the electrode surface, implying that the electrodeposition process takes place in a spherical coordinated way.

In Fig. 4c, the nanostructured Ni deposit from ethaline is efficiently deposited, forming a flower with needles, and a tight, intense surface, and covering the graphite electrode surface zones, as seen in the SEM image.

Elemental composition analysis

The EDX spectrum for Ni nanoparticles from ethaline bath can be seen in Fig. 5b, which reflects the characteristic peak of Ni, verifying the appearance of a pure Ni with an atomic percentage and weight percentage of 100, while in Fig. 5a the EDX spectrum for Ni nanoparticles from acetate gives

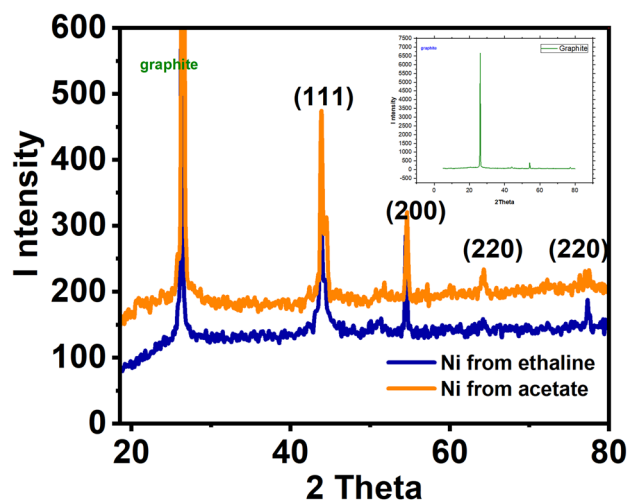
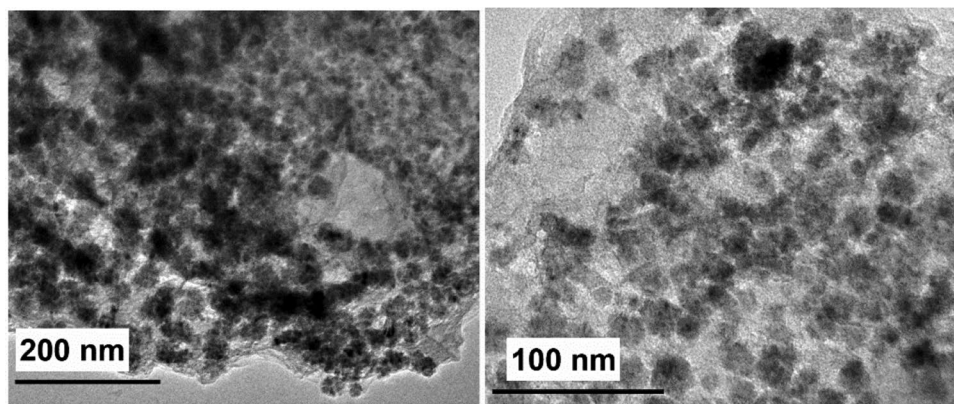


Fig. 6 XRD for fabricated Ni/PGE from ethaline and acetate bath. The inset of the graph corresponds to XRD for bare PGE

Fig. 7 TEM images of the deposited Ni nanoparticles from ethaline with different magnifications



the characteristic peak of Ni with an atomic percentage of 84.22% and weight percentage of 95.14%. Moreover, the appearance of a characteristic peak of oxygen with an atomic percentage of 15.78% and weight percentage of 4.86% may be a result of the oxidation of the Ni nanoparticles. These high mass and atomic percentages of Ni peaks indicate that Ni electrodeposition from ethaline and acetate bath is a successful process. The elemental composition of each characteristic peak of the deposit is tabulated in Table 2.

XRD and TEM analysis

X-ray diffraction had been used to establish the crystalline nature and crystallite size. The XRD of both fabricated Ni from acetate and ethaline solvents can be seen in Fig. 6, which includes three diffraction patterns for the bare graphite electrode at a 2θ value of 26° with high intensity; the XRD of both fabricated Ni from acetate and ethaline solvents is shown in Fig. 6 that contains three diffraction peaks for the electrodeposited Ni from acetate at 2θ values of 44.4° , 52.2° , and 64.2° which refer to diffraction planes (111), (200), and (220) respectively according to JCPDS card no. 041–0850. It is remarkable that the presence of different phases like (220) plane corresponds to NiO but with a small intensity and this is confirmed by EDX which

provides a small characteristic peak of oxygen, while the predominant phase with high intensity relates to diffraction plan (111). Furthermore, the Ni deposit from ethaline exhibits three diffraction peaks at 2θ values of 44.4° , 52.2° , and 77.2° that correlate to diffraction planes (111) with the highest intensity, (200), and (220), suggesting that Ni has an FCC shape [47, 48]. As presented, the diffraction peaks of nanostructured Ni deposit from ethaline perform a lower intensity which suggests and validates the small size of its crystallite particles [47]. According to the Scherrer equation (Eq. 4), the crystallite sizes for the produced Ni deposit from acetate and ethaline were 28 nm and 20 nm, respectively.

$$D = K\lambda/\beta\cos\theta \quad (4)$$

where D represents the crystallite size in nm, K (0.9) is the Scherrer constant, λ is the wavelength of incident X-ray (0.15406 nm), and β represents the radian value of width at half height of the peak [48].

Transmission electron microscopy (TEM) was used to show the Ni film morphology details and their geometric shape as shown in Fig. 7. TEM image of the fabricated Ni electrode from ethaline shows that a metallic Ni has a cubic shape. Figure 8 shows the internal morphology details of

Fig. 8 TEM images of the deposited Ni nanoparticles from acetate with different magnifications

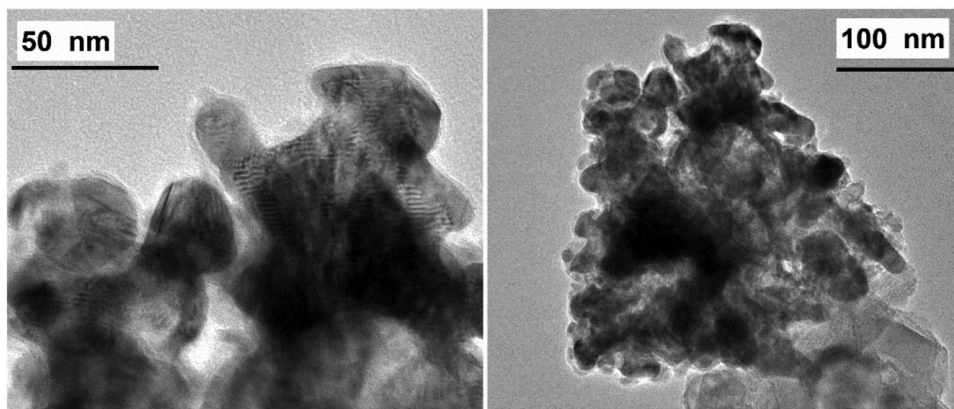
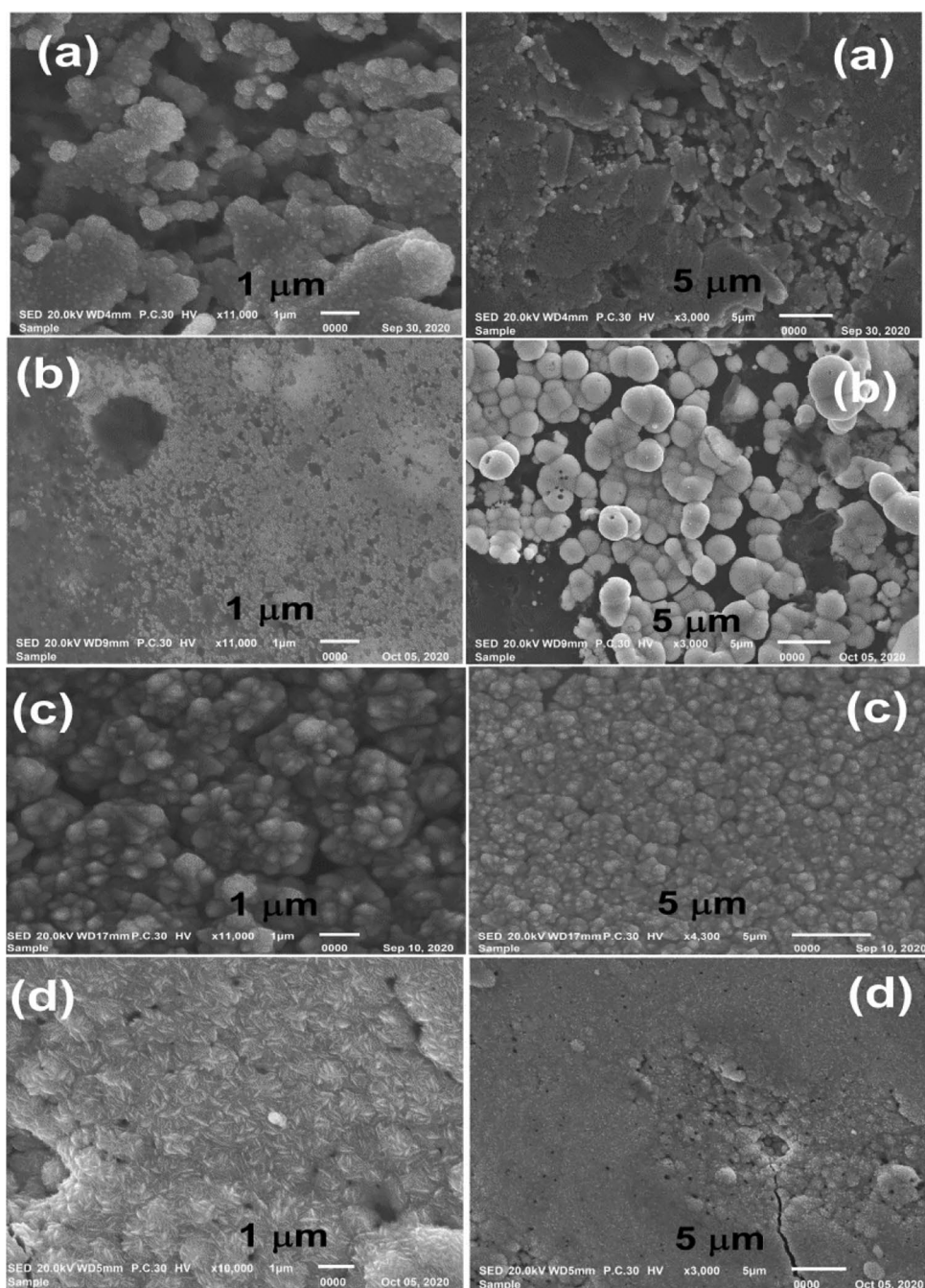


Fig. 9 a–d SEM images of the fabricated Ni nanoparticles from acetate buffer with different pH at a deposition potential of -1.1 V for 900 s



fabricated Ni nanoparticles from acetate with different magnifications which provides a spherical shape of these particles.

pH optimization of Ni nanoparticle electrodeposition from acetate buffer

The pH of the electroplating bath is very important to be controlled to reduce the pitting of the deposit by the hydrogen evolution and also changes the morphology of the

deposit and its catalytic activity. Figure 9a–d show the SEM images of the deposited Ni nanoparticles from different pH of acetate buffer with different magnification scales. Figure 9a represents the SEM images of the deposited Ni nanoparticles from acetate bath at pH 3; the images show uneven surface with coarse grain particles because of the agglomeration of the spherical particles. By increasing the pH value to 4.6 (b), the images show porous spherical particles with pitting due to the hydrogen gas evolution because at low pH the overpotential of the hydrogen evolution reaction is decreased providing the hydrogen gas evolution which

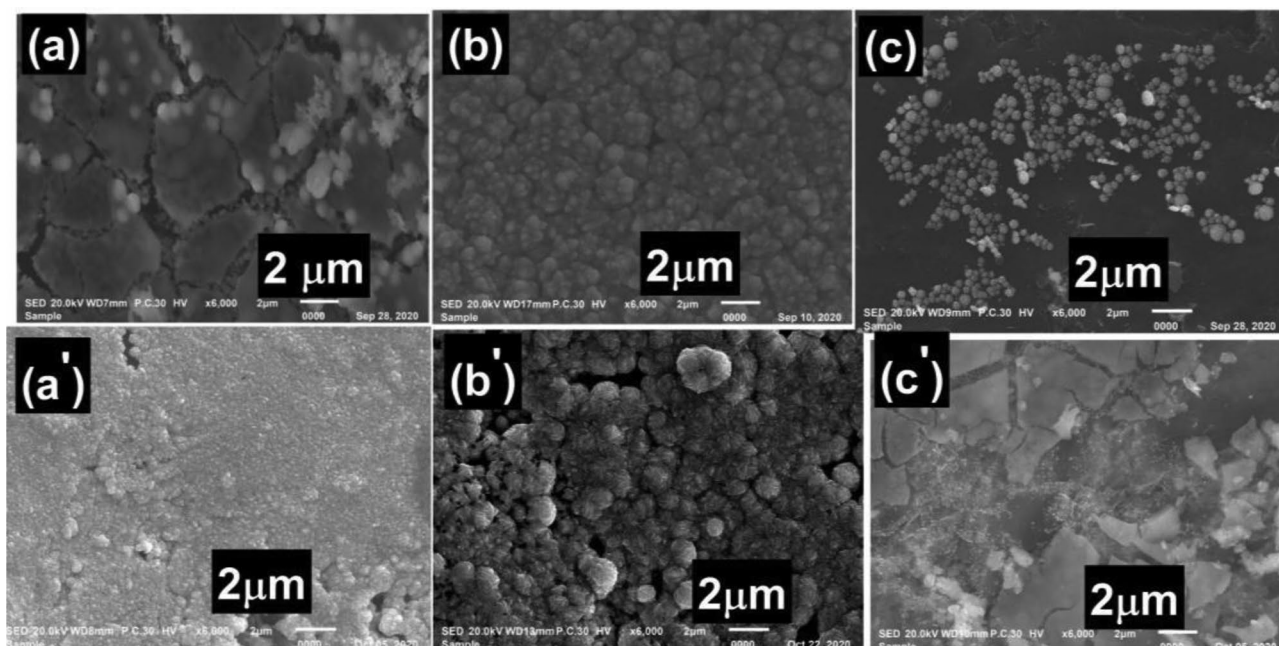


Fig. 10 SEM images of **a–c** fabricated electrodes by Ni nanoparticles from acetate with pH 5.8 at room temperature for 900 s at different deposition potentials (-0.96 V, -1.1 V, and -1.3 V, respectively)

and **a'–c'** fabricated electrodes by Ni nanoparticles from ethaline at 318 K for 900 s at different deposition potentials (-0.85 V, -0.98 V, and -1.16 V, respectively)

adsorbed at the cathode surface, decreasing the active sites of the Ni nucleation [49]. Furthermore, by increasing the pH to a high value of 5.8 (c), the surface becomes more uniform with fine distributed particles forming a cauliflower shape that gives higher catalytic behavior of Ni nanoparticles. At very high pH value 8.5 (d), the particles become very high soft with oval-rod structure with cracking surface.

Electrodeposition potential optimization of Ni nanoparticles from acetate and ethaline solvents

The deposition potential varies from two distinct baths, so various morphologies and catalytic efficiency were obtained. It was discovered that shifting the reduction potential to more

negative values in two distinct baths with the same amplitude provides various morphologies and characteristics of the deposit resulting in different catalytic properties towards HER. Figure 10a–c exhibit SEM images of Ni deposits from an acetate bath with pH 5.8 at room temperature for 900 s at different cathodic potentials (-0.96 V, -1.1 V, and -1.3 V). The Ni deposit at a potential of -0.96 V (a) has a star shape that changes to a homogeneous cauliflower structure when the potential is increased to -1.1 V (b). The particles agglomerate and their sizes grow as the potential increases, as seen in Fig. 6 at a potential of -1.3 V (c), where the particles become spherical like a ball with a bigger size and are not evenly dispersed. Figure 10a'–c' depict the various geometries and morphologies of Ni films deposited from

Fig. 11 **a** Polarization curves of HER in 1 M KOH at a scan rate of 50 mV s^{-1} at fabricated Ni@PGE deposit from ethaline at a potential of -0.98 V and 318 K, and fabricated Ni@PGE from acetate with pH 5.8 at a potential of -1.1 V and bare PGE. **b** Tafel plots for the polarization curves of HER for different modified electrodes

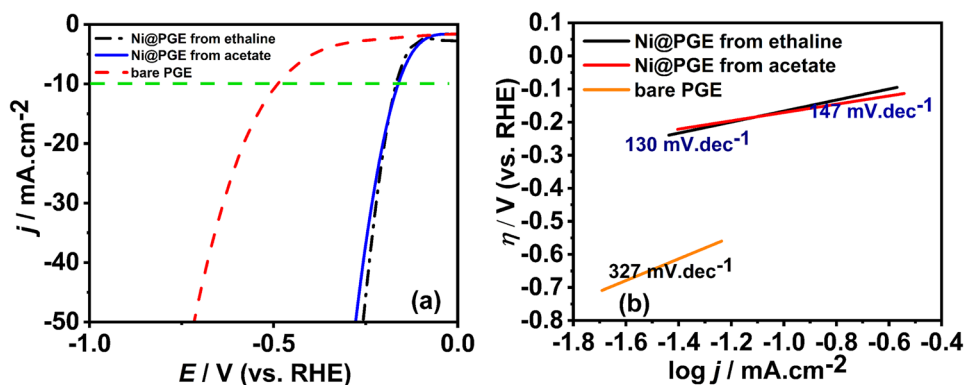


Table 3 Overpotential values for HER, Tafel slopes, and kinetics parameters for different fabricated electrodes in 1 M KOH at room temperature and a scan rate of 50 mV s^{-1}

Ni films	η_{10} (mV)	Tafel slopes (mV dec ⁻¹)	j_0 (A cm ⁻²)	α
Ni@PGE from acetate	-164	147	7.7×10^{-4}	0.20
Ni@PGE from ethaline	-154	130	8.3×10^{-4}	0.22
Bare PGE	-490	327	3.3×10^{-4}	0.09

ethaline at 318 K for 900 s. The deposition at a potential of -0.85 V appears smooth nodular grains by increasing the cathodic potential to -0.98 V ; Ni coatings become well distributed with a uniform needle flower shape filling the surface very well, and then, the particles agglomerate gradually at a high overpotential of -1.16 V forming large particles with random distribution [50] as a fractured layer stuck together. Ni coatings have large particles at a cathodic potential of -1.16 V because of the high overpotential that accelerates the growth rate and this observation agrees with the observation of Wang et al. [51]. The various deposition potentials disclose various morphologies and structures, as can be observed. Additionally, the varied morphologies revealed and confirmed distinct catalytic activity towards HER after deposition from two different baths [52, 53].

Comparison between the electrocatalytic activities of fabricated Ni nanoparticles at PGE from acetate and ethaline for HER

Figure 11a shows linear sweep voltammetry (LSV) in 1 M KOH for HER at a scan rate of 50 mV s^{-1} by fabricated Ni nanoparticles at PGE from acetate, ethaline, and bare electrode. It was found that the bare electrode has the lowest catalytic activity and the highest onset potential among them; at a current density of 10 mA cm^{-2} , it possesses an overpotential (η) of -490 mV vs RHE. Meanwhile, the fabricated Ni nanoparticles from acetate possess an overpotential of -164 mV at a current density of 10 mA cm^{-2} and the fabricated Ni nanoparticles from ethaline only requires an overpotential of -154 mV to reach 10 mA cm^{-2} , which means the highest catalytic activity of Ni nanoparticle deposit from ethaline compared with the other fabricated Ni electrode from acetate, while the bare electrode is inactive towards HER. Figure 11b shows the Tafel plots of different modified electrodes; the Ni nanoparticle deposit from ethaline has the lowest Tafel slope of 130 mV dec^{-1} , while the Tafel slopes for Ni nanoparticle deposit from acetate and bare PGE are 147 and 327 mV dec^{-1} , respectively, suggesting that the fabricated nanoparticle Ni@PGE from ethaline has the highest catalytic activity and the fastest kinetics for HER compared to the other electrodes. The kinetics parameters were

Fig. 12 **a** CV curves in 1 M KOH at the non-faradic regions of the deposited nano-Ni film from acetate. **b** CV curves in 1 M KOH at the non-faradic regions of the deposited nano-Ni film from ethaline. **c** The capacitive current relation as a function of scan rates for fabricated Ni@PGE from ethaline and fabricated Ni@PGE from acetate

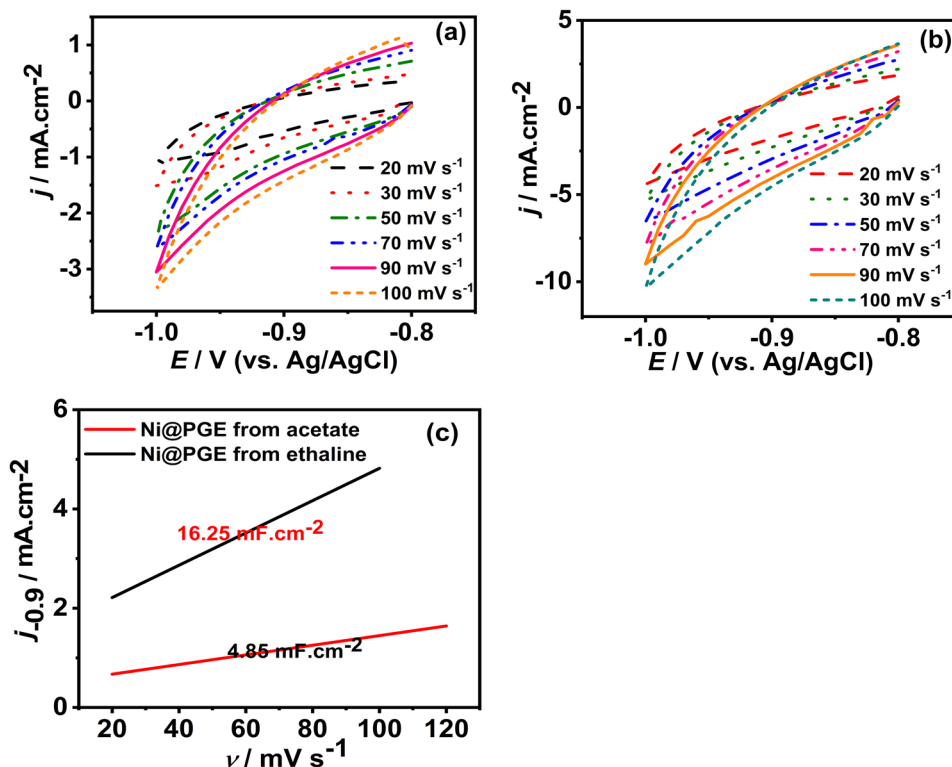


Table 4 Comparison between the catalytic parameters for different catalysts for HER

Catalyst	Medium	η_{10} (mV)	Scan rate (mV s ⁻¹)	Reference
CoNi-30	1 M KOH	-210	5	[55]
NiCo ₂ S ₄ NW/NF arrays	1 M KOH	-210	10	[56]
Porous Ni	1 M KOH	114	50	[57]
Pt/Ni-SP	1 M NaOH	250	50	[58]
Ni@PGE nanoparticles from acetate	1 M KOH	-164	50	This work
Ni@PGE nanoflower from ethaline	1 M KOH	-154	50	This work

calculated from the Tafel plots for both Ni deposits from the two different mediums towards HER. The most vital kinetic parameter which is the exchanging current density (j_0) has been calculated and is found to be 8.3×10^{-4} A cm⁻² for the fabricated Ni nanoparticles from ethaline, 7.7×10^{-4} A cm⁻² for the fabricated Ni nanoparticles from acetate, and 3.3×10^{-4} A cm⁻² for the bare PGE. As shown from the previous results, the fabrication of Ni nanoparticles at PGE from ethaline has the highest j_0 and α indicating its higher catalytic activity towards HER due to its high surface area according to its needle flower morphology which possesses more active sites and its smaller size.

Table 3 represents the comparison of overpotentials, Tafel slopes, and kinetics parameters between the different modified electrodes.

The ECSA is proportional to the capacitance double layer (C_{dl}) which is evaluated in the non-faradic region of HER or OER at different scan rates. CV measurements of the two different fabricated Ni nanoparticle electrodes from acetate and ethaline in the non-faradic region of HER were estimated in 1 M KOH at 298 K at different scan rates (20, 30, 50, 70, 90, and 100 mV s⁻¹) as has been seen in Fig. 12a and b. Figure 12c shows the linear relationship of the difference between charging and discharging current density which is chosen at the constant potential in the middle distance between the initial and final potential (-0.9 V vs. Ag/AgCl) against the different scan rates; half of the slope is the capacitance double layer (C_{dl}) [54] which is higher four times for the fabricated Ni nanostructure deposit from ethaline compared with the other fabricated Ni nanoparticle electrode from acetate, suggesting its higher catalytic activity towards HER. The

comparison between kinetics parameters and Tafel slopes for different Ni-based catalysts and our present work is summarized in Table 4.

As has been shown in Table 4, the deposited Ni@PGE from ethaline has a small negative overpotential value towards HER compared with other bifunctional catalysts like CoNi-30 and NiCo₂S₄ NW/NF arrays which proves the activity of the deposited Ni nanoparticles from DES and opens a new approach for improving a new bifunctional catalyst from DES towards HER. The overpotential value of the deposited Ni nanoparticles was compared with other researches that used the commercial Pt/C catalysts towards HER. It was found that Pt/C catalyst with high loading of 340 mg cm⁻² possesses a lower overpotential value of 53 mV to achieve a current density of 10 mA cm⁻², while the deposited Ni nanoparticles from ethaline with lower loading of 0.018 mg cm⁻² with higher mass activity of 333.3 mA mg⁻¹ than the Pt/C catalyst of 330 mA mg⁻¹ possess a higher overpotential value of -154 mV to achieve a current density of 10 mA cm⁻². Table 5 contains the comparison between different commercial Pt/C catalyst loading and Ni nanoparticles from ethaline solvent in terms of overpotential values and Tafel slope for HER. Despite the higher overpotential value for Ni nanoflowers than Pt/C, Ni nanoparticle deposit from DES provides a remarkable enhancement in the electrocatalytic activity towards HER with low loading, while the Pt/C possesses a smaller overpotential value in the case of high loading of the catalyst.

Furthermore, the durability and stability of the fabricated Ni deposit from ethaline were studied in 1 M KOH after 1000 cycles and chronoamperometry for 4500 s.

Table 5 Comparison between the catalytic activity of commercial Pt/C catalysts and nanostructure Ni@PGE deposit from ethaline for HER

Catalysts	Mass activity	Catalyst loading (mg cm ⁻²)	Overpotential (η) mV	Tafel slope (mV dec ⁻¹)	References
Pt/C	330	340	53	-	[58]
Pt/C/NF	-	18.6	-20	30.6	[34]
Pt/C	-	-	-30	63	[55]
Ni@PGE nanoflower from ethaline	333.3	0.018	-154	130	This work

Fig. 13 **a** The chronoamperometry time–current curve for deposited Ni from ethaline at onset pot -1.1 V vs Ag/AgCl (3 M KCl). **b** Polarization curves for HER in 1 M KOH after 1 cycle and 1000 cycles for deposited Ni from ethaline

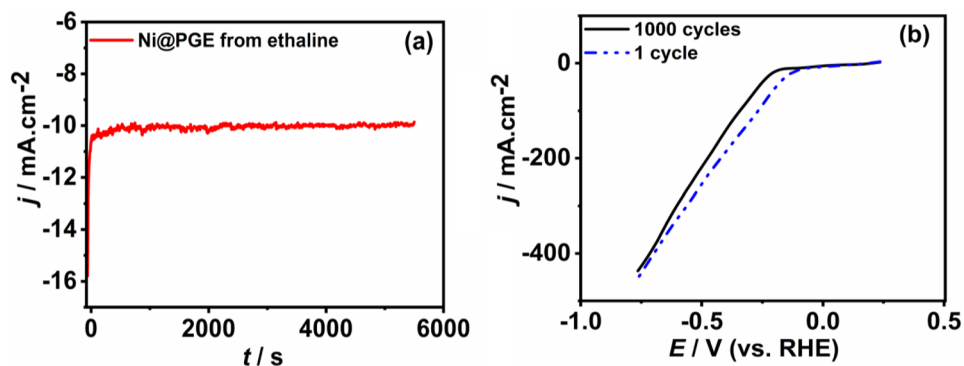


Fig. 14 **a** Polarization curves of OER in 1 M KOH at a scan rate of 50 mV s^{-1} at room temperature at fabricated Ni@PGE deposit from ethaline at a potential of -0.98 V and 318 K, and fabricated Ni@PGE from acetate with pH 5.8 at a potential of -1.1 V and bare PGE. **b** Tafel plots for the polarization curves of OER for the different three electrodes

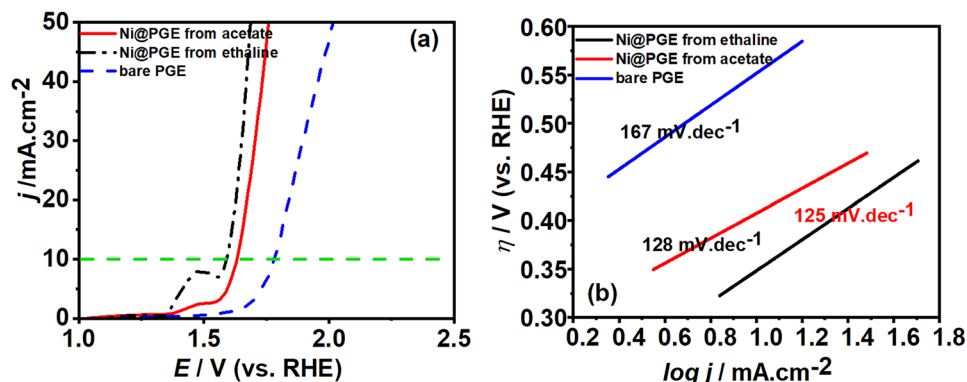


Figure 13a shows good stability as the current is retained of 63% of its initial current. While the LSV for HER after 1 cycle and 1000 cycles has been studied to show its durability, as has been shown in Fig. 13b, its catalytic activity drops after 1000 cycles which means that the stability of nano-Ni deposit from ethaline for HER needs to be improved.

The electrocatalytic activity of fabricated Ni nanoparticles at PGE from acetate and ethaline for OER

Further investigations were estimated for both fabricated Ni electrocatalysts from acetate and ethaline for the oxygen evolution reaction (OER). Figure 14a represents LSV polarization curves in 1 M KOH at room temperature at a scan rate of 50 mV s^{-1} for OER at deposited Ni nanoparticles from acetate bath with pH 5.8 at a potential of -1.1 V and ethaline bath at a potential of -0.98 V and temperature 318 K; it shows that electrodeposited Ni nanoparticle electrocatalyst from ethaline has an overpotential of 350 mV to reach the current density of 10 mA cm^{-2} , while the electrodeposited Ni nanoparticles from acetate and bare PGE have an overpotential of 400 mV and 550 mV to reach the current density of 10 mA cm^{-2} . Remarkably, there is an oxidation peak which refers to the oxidation of Ni nanoparticles to Ni^{+2} due to the formation of nickel oxyhydroxide (NiOOH) in the alkaline

medium which performed as active species to enhance the electrocatalytic activity for OER [34]. From these results, it is clear that the fabricated Ni nanoparticle electrocatalyst from ethaline has the lowest overpotential towards OER and hence the best catalytic activity. Figure 14b shows the Tafel plots of different modified electrodes for OER; the deposited Ni nanoparticles from ethaline own the lowest Tafel slope of 125 mV dec^{-1} while the Tafel slopes for deposited Ni nanoparticles from acetate and bare PGE are 128 and 167 mV dec^{-1} , respectively, indicating that fabricated PGE with Ni nanoparticles from ethaline has more active sites and the fastest kinetics for OER compared with the other electrodes [55].

The kinetics parameters were calculated for each electrode for OER in Table 6 that shows the fabricated Ni nanoparticle electrode from ethaline has the highest j_0 and α value and the lowest overpotential means that it has the best kinetics for OER.

Table 6 Values of overpotential, Tafel slopes, and kinetics parameters for different fabricated electrodes in 1 M KOH at room temperature at a scan rate of 50 mV s^{-1} in the case of OER

Ni films	η_{10} (mV)	Tafel slopes (mV dec^{-1})	j_0 (A.cm^{-2})	α
Ni@PGE from acetate	400	128	12.6×10^{-2}	0.230
Ni@PGE from ethaline	350	125	14.4×10^{-2}	0.236
Bare PGE	550	167	2.33×10^{-2}	0.176

Fig. 15 **a** CV curves at the non-faradic regions (−0.2 V to 0.4 V) vs Ag/AgCl (3 M KCl) of the deposited nano-Ni film from acetate. **b** CV curves at the non-faradic regions (−0.2 V to 0.4 V) vs Ag/AgCl (3 M KCl) of deposited Ni-nano film from ethaline. **c** The capacitive current relation as a function of scan rate for fabricated Ni@PGE from ethaline and fabricated Ni@PGE from acetate

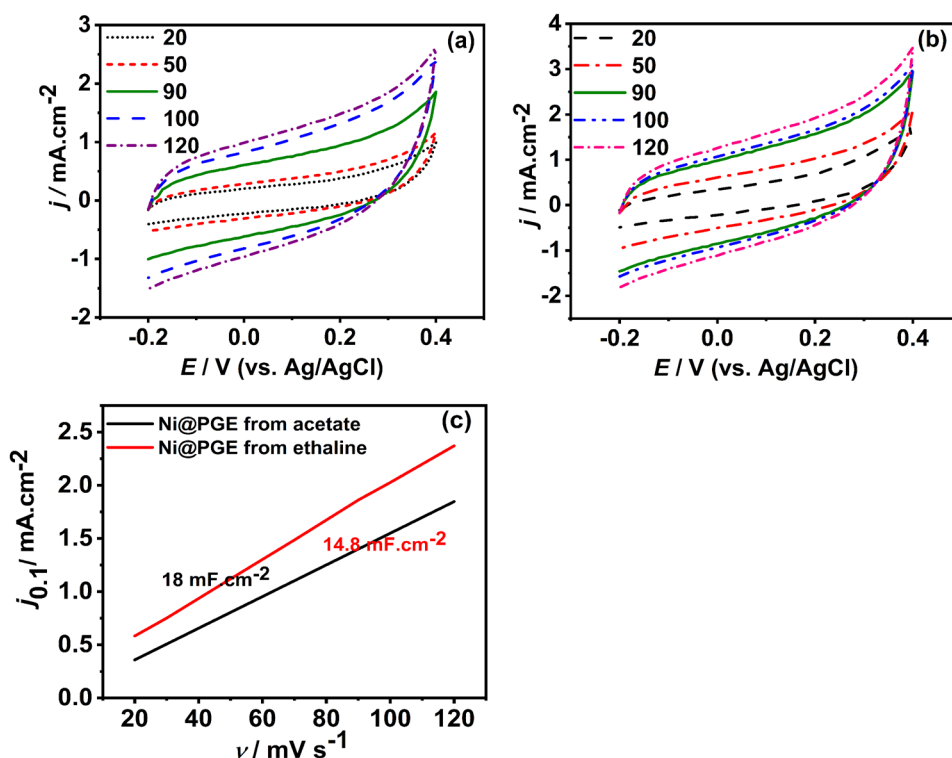


Figure 15a and b show the CV measurements of deposited Ni nanoparticles from acetate and ethaline, respectively, in 1 M KOH in the non-faradic region of OER at different scan rates to calculate the C_{dl} for both catalysts. Figure 15c represents that fabricated Ni nanoparticles from ethaline own the highest C_{dl} which equals to 18 mF cm^{-2} , while the fabricated Ni nanoparticles from acetate possess 14.8 mF cm^{-2} , suggesting that Ni nanoparticle deposit from ethaline has higher ECSA and catalytic activity compared with the fabricated Ni nanoparticle deposit from the acetate. The results of j_0 of the fabricated Ni from ethaline for HER and OER were compared and show that Ni nanoparticles from ethaline have higher kinetics for OER than for HER.

The comparison of kinetics parameters and Tafel slopes for different Ni-based catalysts and our work is summarized in Table 7.

The overpotential value of the deposited Ni nanoparticles was compared with other researches that used the commercial IrO_2 and RuO_2 catalysts towards OER in Table 8. The deposited Ni nanoflowers from ethaline with very small loading present a smaller Tafel slope of 125 mV dec^{-1} than the RuO_2/NF which exhibits $129.1 \text{ mV dec}^{-1}$ with higher loading, suggesting its promoting catalytic activity towards OER.

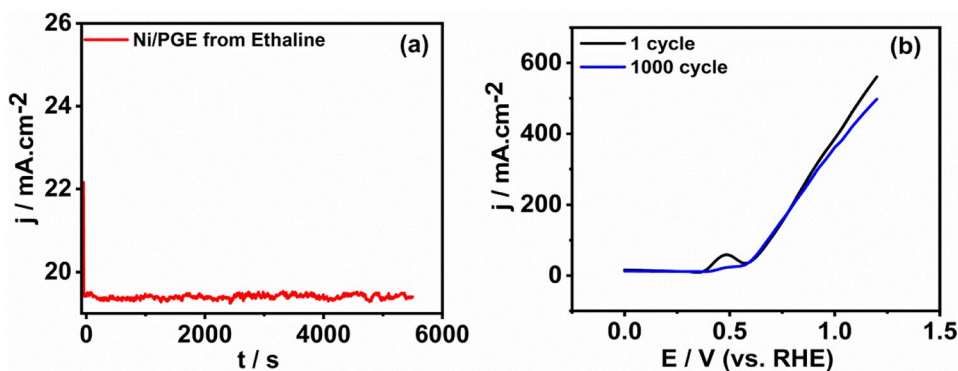
Figure 16a and b demonstrate the durability and stability of the deposited Ni nanoparticles from ethaline in 1 M KOH. It shows that the catalyst has excellent mechanical properties and stability towards OER as the current is retained at 86% of its initial current, unlike HER. The LSV after 1 cycle and 1000 cycles does not change and is almost the same which demonstrates that it has long-term durability compared with its stability and durability in the case of HER.

Table 7 Comparison of the overpotential values for different Ni-based catalysts for OER

Catalyst	Medium	η_{10} (mV)	Scan rate (mV s ⁻¹)	Reference
Ni Fe Al O with metal vacancies	1 M NaOH	371	10	[59]
SFOCI catalyst	1 M KOH	1720@10 mA cm ⁻²	50	[60]
Fe doped NiP	1 M KOH	270 @20 mA cm ⁻²	50	[61]
Fe doped Ni(OH) ₂ /Ni foam	1 M KOH	271 @20 mA cm ⁻²	2	[62]
Nanoflower Ni from DES	1 M KOH	350	50	This work
Ni nanoparticles from acetate	1 M KOH	400	50	This work

Table 8 Comparison between the catalytic activities of commercial RuO₂ and IrO₂ catalysts and nanostructure Ni/PGE deposit from ethaline for OER

Catalysts	Mass activity	Catalyst loading (mg cm ⁻²)	Overpotential (η) mV	Tafel slope (mV dec ⁻¹)	References
RuO ₂ /NF	-	2.8	140	90.1	[63]
RuO ₂ /NF	-	18.6	-	129.1	[34]
IrO ₂	-	-	270	110	[55]
Ni/PGE nanoflower from ethaline	333.3	0.018	350	125	This work

Fig. 16 **a** The chronoamperometry time–current curve for deposited Ni from ethaline at onset pot 1.59 V vs Ag/AgCl (3 M KCl). **b** Polarization curves for OER in 1 M KOH after 1 cycle and 1000 cycles for deposited Ni from ethaline

Conclusions

The electrodeposition process of Ni from DES is more effective than from the aqueous solvent and produces more fine Ni nanoparticles with a uniform needle flower structure with a small size of 20 nm which has more active sites for HER and OER. Furthermore, it has higher catalytic efficiency and kinetics for both HER and OER compared with the deposited Ni nanoparticles from the acetate bath. The fabricated Ni electrode from ethaline has a higher current density, less overpotential for both HER and OER of -154 mV and 350 mV, respectively, and smaller Tafel slope for both HER and OER of 130 mV dec⁻¹ and 125 mV dec⁻¹, respectively, compared with the fabricated Ni electrode from acetate bath which has a high overpotential for both HER and OER of -164 mV and 400 mV, respectively, and higher Tafel slope of 147 mV dec⁻¹ and 128 mV dec⁻¹ for both HER and OER, respectively. The results of j_0 for the deposited Ni nanoparticles from ethaline for HER and OER were compared and show that Ni nanoparticles from ethaline have higher kinetics and higher stability for OER than for HER.

Abbreviations DESs: Deep eutectic solvents; ECSA: Electrochemical surface area; HER: Hydrogen evolution reaction; ChCl: Choline chloride; EG: Ethylene glycol; SEM: Scanning electron microscopy; XRD: X-ray diffraction; EDX: Energy-dispersive X-ray; PGE: Pencil graphite electrode; QRE: Quasi-reference electrode; CV: Cyclic voltammetry; CA: Chronoamperometry; OER: Oxygen evolution reaction; TEM: Transmission electron microscope; PTFE: Polytetrafluoroethylene; NF: Nickel foam; CC: Carbon cloth

Funding Open access funding provided by The Science, Technology & Innovation Funding Authority (STDF) in cooperation with The Egyptian Knowledge Bank (EKB).

Open Access This article is licensed under a Creative Commons Attribution 4.0 International License, which permits use, sharing, adaptation, distribution and reproduction in any medium or format, as long as you give appropriate credit to the original author(s) and the source, provide a link to the Creative Commons licence, and indicate if changes were made. The images or other third party material in this article are included in the article's Creative Commons licence, unless indicated otherwise in a credit line to the material. If material is not included in the article's Creative Commons licence and your intended use is not permitted by statutory regulation or exceeds the permitted use, you will need to obtain permission directly from the copyright holder. To view a copy of this licence, visit <http://creativecommons.org/licenses/by/4.0/>.

References

- Wei Y, Wang R, Meng L, Wang Y, Li G, Xin S, Zhao X, Zhang K (2017) Hydrogen generation from alkaline NaBH₄ solution using a dandelion-like Co–Mo–B catalyst supported on carbon cloth. *Int J Hydrogen Energy* 42:9945–9951. <https://doi.org/10.1016/j.ijhydene.2016.12.130>
- Wang M, Fu W, Du L, Wei Y, Rao P, Wei L, Zhao X, Wang Y, Sun S, Wang M, Fu W, Du L, Wei Y, Rao P, Wei L, Zhao X, Wang Y, Sun S (2020) Surface engineering by doping manganese into cobalt phosphide towards highly efficient bifunctional HER and OER electrocatalysis. *ApSS* 515:146059. <https://doi.org/10.1016/j.apsusc.2020.146059>
- Rao P, Cui P, Yang L, Wang M, Wang S, Cai H, Wang Y, Zhao X, Wilkinson DP, Zhang J, Rao P, Cui P, Yang L, Wang M, Wang

- S, Cai H, Wang Y, Zhao X, Wilkinson DP, Zhang J (2020) Surface plasma-etching treatment of cobalt nanoparticles-embedded honeysuckle-like nitrogen-doped carbon nanotubes to produce high-performance catalysts for rechargeable zinc-air batteries. *JPS* 453:227858. <https://doi.org/10.1016/J.JPOWSOUR.2020.227858>
4. Wang JG, Hua W, Li M, Liu H, Shao M, Wei B (2018) Structurally engineered hyperbranched NiCoP arrays with superior electrocatalytic activities toward highly efficient overall water splitting. *ACS Appl Mater Interfaces* 10:41237–41245. https://doi.org/10.1021/ACSAMI.8B11576/SUPPL_FILE/AM8B11576_SI_001.PDF
 5. Paul R, Du F, Dai L, Ding Y, Wang ZL, Wei F, Roy A (2019) 3D Heteroatom-doped carbon nanomaterials as multifunctional metal-free catalysts for integrated energy devices. *Adv Mater* 31:1805598. <https://doi.org/10.1002/ADMA.201805598>
 6. Hung SF, Hsu YY, Chang CJ, Hsu CS, Suen NT, Chan TS, Chen HM (2018) Electrocatalysts: unraveling geometrical site confinement in highly efficient iron-doped electrocatalysts toward oxygen evolution reaction (*Adv. Energy Mater.* 7/2018). *Adv Energy Mater* 8:1870032. <https://doi.org/10.1002/AENM.201870032>
 7. El-Hallag I, Elsharkawy S, Hammad S (2022) The effect of electrodeposition potential on catalytic properties of Ni nanoparticles for hydrogen evolution reaction (HER) in alkaline media. *J Appl Electrochem* 1:1–12. <https://doi.org/10.1007/S10800-022-01679-W>
 8. El-Hallag I, Elsharkawy S, Hammad S (2021) Electrodeposition of Ni nanoparticles from deep eutectic solvent and aqueous solution as electrocatalyst for methanol oxidation in acidic media. *Int J Hydrogen Energy* 46:15442–15453. <https://doi.org/10.1016/J.IJHYDENE.2021.02.049>
 9. Patel PP, Hanumantha PJ, Datta MK, Velikokhatnyi OI, Hong D, Poston JA, Manivannan A, Kumta PN (2017) Cobalt based nanostructured alloys: versatile high performance robust hydrogen evolution reaction electro-catalysts for electrolytic and photo-electrochemical water splitting. *Int J Hydrogen Energy* 42:17049–17062. <https://doi.org/10.1016/J.IJHYDENE.2017.05.175>
 10. Wu Y, He H (2018) Direct-current electrodeposition of Ni–S–Fe alloy for hydrogen evolution reaction in alkaline solution. *Int J Hydro Energ* 1989–1997. <https://doi.org/10.1016/J.IJHYDENE.2017.12.015>
 11. Chen L, Dong X, Wang Y, Xia Y (2016) Separating hydrogen and oxygen evolution in alkaline water electrolysis using nickel hydroxide. *Nature Commun* 7:1(7)1–8. <https://doi.org/10.1038/ncomms11741>
 12. Najafpour MM, Renger G, Holyńska M, Moghaddam AN, Aro EM, Carpentier R, Nishihara H, Eaton-Rye JJ, Shen JR, Allakhverdiev SI (2016) Manganese compounds as water-oxidizing catalysts: from the natural water-oxidizing complex to nanosized manganese oxide structures. *Chem Rev* 116:2886–2936. https://doi.org/10.1021/ACS.CHEMREV.5B00340/ASSET/IMAGES/ACS.CHEMREV.5B00340.SOCIAL.JPEG_V03
 13. Cao L, Luo Q, Liu W, Lin Y, Liu X, Cao Y, Zhang W, Wu Y, Yang J, Yao T, Wei S (2018) Identification of single-atom active sites in carbon-based cobalt catalysts during electrocatalytic hydrogen evolution. *Nat Catal* 2:2(2)134–141. <https://doi.org/10.1038/s41929-018-0203-5>
 14. Yu F, Zhou H, Huang Y, Sun J, Qin F, Bao J, Goddard WA, Chen S, Ren Z (2018) High-performance bifunctional porous non-noble metal phosphide catalyst for overall water splitting. *Nat Commun* 9:1(9)1–9. <https://doi.org/10.1038/s41467-018-04746-z>
 15. Wei Y, Huang X, Wang J, Yu H, Zhao X, Cheng D (2017) Synthesis of bifunctional non-noble monolithic catalyst Co-W-P/carbon cloth for sodium borohydride hydrolysis and reduction of 4-nitrophenol. *Int J Hydrogen Energy* 42:25860–25868. <https://doi.org/10.1016/J.IJHYDENE.2017.08.148>
 16. Shedid MH, Elshokary S, Shedid MH, Elshokary S (2015) Hydrogen production from an alkali electrolyzer operating with Egypt natural resources. *Smart Grid and Renewable. Energy* 6:14–25. <https://doi.org/10.4236/SGRE.2015.61002>
 17. Wang L, Wen B, Bai X, Liu C, Yang H (2019) NiCo Alloy/Carbon nanorods decorated with carbon nanotubes for microwave absorption. *ACS Applied Nano Materials* 2:7827–7838. https://doi.org/10.1021/ACSANM.9B01842/SUPPL_FILE/AN9B01842_SI_001.PDF
 18. Li S, Sirisomboonchai S, Yoshida A, An X, Hao X, Abudula A, Guan G (2018) Bifunctional CoNi/CoFe₂O₄/Ni foam electrodes for efficient overall water splitting at a high current density. *J Mater Chem A* 6:19221–19230. <https://doi.org/10.1039/C8TA08223E>
 19. Yu J, Cao Q, Li Y, Long X, Yang S, Clark JK, Nakabayashi M, Shibata N, Delaunay JJ (2019) Defect-rich NiCeOx electrocatalyst with ultrahigh stability and low overpotential for water oxidation. *ACS Catal* 9:1605–1611. https://doi.org/10.1021/ACSCATAL.9B00191/SUPPL_FILE/CS9B00191_SI_001.PDF
 20. Li Y, Huang B, Sun Y, Luo M, Yang Y, Qin Y, Wang L, Li C, Lv F, Zhang W, Guo S, Li YJ, Sun YJ, Luo MC, Yang Y, Qin YN, Li CJ, Lv F, Zhang WY, Guo SJ, Huang BL, Wang L (2019) Multi-metal borides nanochains as efficient electrocatalysts for overall water splitting. *Small* 15:1804212. <https://doi.org/10.1002/SMLL.201804212>
 21. Davodi F, Mühlhausen E, Tavakkoli M, Sainio J, Jiang H, Gökce B, Marzun G, Kallio T (2018) Catalyst support effect on the activity and durability of magnetic nanoparticles: toward design of advanced electrocatalyst for full water splitting. *ACS Appl Mater Interfaces* 10:31300–31311. https://doi.org/10.1021/ACSAMI.8B08830/SUPPL_FILE/AM8B08830_SI_001.PDF
 22. He Y, Han XP, Rao DW, Zhang YD, Zhao J, Zhong C, Bin Hu W, Wei WF, da Deng Y (2019) Charge redistribution of Co on cobalt (II) oxide surface for enhanced oxygen evolution electrocatalysis. *Nano Energ* 61:267–274. <https://doi.org/10.1016/J.NANOEN.2019.04.077>
 23. Liu D, Dai L, Lin X, Chen JF, Zhang J, Feng X, Müllen K, Zhu X, Dai S (2019) Chemical approaches to carbon-based metal-free catalysts. *Adv Mater* 31:1804863. <https://doi.org/10.1002/ADMA.201804863>
 24. Mahmood J, Anjum MAR, Shin SH, Ahmad I, Noh HJ, Kim SJ, Jeong HY, Lee JS, Baek JB (2018) Encapsulating iridium nanoparticles inside a 3D cage-like organic network as an efficient and durable catalyst for the hydrogen evolution reaction. *Adv Mater* 30:1805606. <https://doi.org/10.1002/ADMA.201805606>
 25. Wei Y, Meng W, Wang Y, Gao Y, Qi K, Zhang K (2017) Fast hydrogen generation from NaBH₄ hydrolysis catalyzed by nanostructured Co–Ni–B catalysts. *Int J Hydrogen Energy* 42:6072–6079. <https://doi.org/10.1016/J.IJHYDENE.2016.11.134>
 26. Xiao Y, Zhang P, Zhang X, Dai X, Ma Y, Wang Y, Jiang Y, Liu M, Wang Y (2017) Bimetallic thin film NiCo–NiCoO₂@NC as a superior bifunctional electrocatalyst for overall water splitting in alkaline media. *Journal of Materials Chemistry A* 5:15901–15912. <https://doi.org/10.1039/C7TA03629A>
 27. Gund GS, Dubal DP, Shinde SS, Lokhande CD (2013) One step hydrothermal synthesis of micro-belts like β-Ni(OH)₂ thin films for supercapacitors. *Ceram Int* 39:7255–7261. <https://doi.org/10.1016/J.CERAMINT.2013.01.091>
 28. Dubal DP, Gomez-Romero P, Sankapal BR, Holze R (2015) Nickel cobaltite as an emerging material for supercapacitors: an overview. *Nano Energy* 11:377–399. <https://doi.org/10.1016/J.NANOEN.2014.11.013>
 29. Gund GS, Dubal DP, Shinde SS, Lokhande CD (2014) Architected morphologies of chemically prepared NiO/MWCNTs nano-hybrid thin films for high performance supercapacitors. *ACS Appl*

- Mater Interfaces 6:3176–3188. https://doi.org/10.1021/AM404422G/SUPPL_FILE/AM404422G_SI_001.PDF
30. Gong M, Wang DY, Chen CC, Hwang BJ, Dai H (2015) A mini review on nickel-based electrocatalysts for alkaline hydrogen evolution reaction. *Nano Res* 9:1(9)28–46. <https://doi.org/10.1007/S12274-015-0965-X>
 31. Yu X, Zhao J, Zheng LR, Tong Y, Zhang M, Xu G, Li C, Ma J, Shi G (2018) Hydrogen evolution reaction in alkaline media: alpha- or beta-nickel hydroxide on the surface of platinum? *ACS Energy Lett* 3:237–244. https://doi.org/10.1021/ACSENERGYL.ETT.7B01103/SUPPL_FILE/NZ7B01103_SI_001.PDF
 32. Balram A, Zhang H, Santhanagopalan S (2017) In situ decoration of stainless steel nanoparticles for synergistic enhancement of α -Ni(OH)₂ oxygen evolution reaction catalysis, *Materials Chemistry Frontiers* 1:2376–2382. <https://doi.org/10.1039/C7QM00299H>
 33. Jin C, Zhou N, Wang Y, Li X, Chen M, Dong Y, Yu Z, Liang Y, Qu D, Dong Y, Xie Z, Zhang C (2020) 3D porous and self-supporting Ni foam@graphene@Ni₃S₂ as a bifunctional electrocatalyst for overall water splitting in alkaline solution. *J Electroanal Chem* 858. <https://doi.org/10.1016/J.JELECHEM.2019.113795>
 34. Yao K, Zhai M, Ni Y (2019) α -Ni(OH)₂ · 0.75H₂O nanofilms on Ni foam from simple NiCl₂ solution: fast electrodeposition, formation mechanism and application as an efficient bifunctional electrocatalyst for overall water splitting in alkaline solution. *Electrochimica Acta* 301:87–96. <https://doi.org/10.1016/J.ELECTACTA.2019.01.152>
 35. Abbott AP, Capper G, Davies DL, Rasheed RK, Tambyrajah V (2003) Novel solvent properties of choline chloride/urea mixtures. *Chem Commun* 70–71. <https://doi.org/10.1039/B210714G>
 36. Smith EL, Abbott AP, Ryder KS (2014) Deep eutectic solvents (DESs) and their applications. *Chem Rev* 114:11060–11082. https://doi.org/10.1021/CR300162P/ASSET/IMAGES/CR300162P_SOCIAL.JPEG_V03
 37. Endres F, MacFarlane D, Abbott A (2008) Electrodeposition from ionic liquids, *electrodeposition from ionic liquids*. 1–387. <https://doi.org/10.1002/9783527622917>
 38. Mernissi Cherigui EA, Sentosun K, Bouckennoog P, Vanrompay H, Bals S, Terryn H, Ustarroz J (2017) comprehensive study of the electrodeposition of nickel nanostructures from deep eutectic solvents: self-limiting growth by electrolysis of residual water. *J Phys Chem C* 121:9337–9347. https://doi.org/10.1021/ACS.JPCC.7B01104/SUPPL_FILE/JP7B01104_SI_001.PDF
 39. Costovici S, Manea AC, Visan T, Anicai L (2016) Investigation of Ni-Mo and Co-Mo alloys electrodeposition involving choline chloride based ionic liquids. *Electrochim Acta* 207:97–111. <https://doi.org/10.1016/J.ELECTACTA.2016.04.173>
 40. Wang J, Xu F, Jin H, Chen Y, Wang Y (2017) Non-noble metal-based carbon composites in hydrogen evolution reaction: fundamentals to applications. *Adv Mater* 29:1605838. <https://doi.org/10.1002/ADMA.201605838>
 41. Maniam KK, Paul S (2020) Progress in electrodeposition of zinc and zinc nickel alloys using ionic liquids. *Appl Sci (Switzerland)* 10. <https://doi.org/10.3390/APP10155321>
 42. *Electrochemical methods: fundamentals and applications*, 2nd Edition | Wiley (n.d.). <https://www.wiley.com/en-us/Electrochemical+Methods%3A+Fundamentals+and+Applications%2C+2nd+Edition-p-9780471043720>. Accessed 30 Mar 2022
 43. Jiang T, Chollier Brym MJ, Dubé G, Lasia A, Brisard GM (2006) Electrodeposition of aluminium from ionic liquids: Part II - studies on the electrodeposition of aluminum from aluminum chloride (AlCl₃) - trimethylphenylammonium chloride (TMPAC) ionic liquids. *Surf Coat Technol* 201:10–18. <https://doi.org/10.1016/J.SURFCOAT.2005.12.024>
 44. Abbott AP, el Ttaib K, Frisch G, McKenzie KJ, Ryder KS (2009) Electrodeposition of copper composites from deep eutectic solvents based on choline chloride. *Phys Chem Chem Phys* 11:4269–4277. <https://doi.org/10.1039/B817881J>
 45. Electrodeposition of aluminium from ionic liquids: Part I—electrodeposition and surface morphology of aluminium from aluminium chloride (AlCl₃)–1-ethyl-3-methylimidazolium chloride ([EMIm]Cl) ionic liquids | Andrzej Lasia - Academia.edu, (n.d.). https://www.academia.edu/23565293/Electrodeposition_of_aluminium_from_ionic_liquids_Part_I_electrodeposition_and_surface_morphology_of_aluminium_from_aluminium_chloride_AlCl3_1-ethyl-3-methylimidazolium_chloride_EMIm_Cl_ionic_liquids. Accessed 30 Mar 2022
 46. Wang S, Zou X, Lu Y, Rao S, Xie X, Pang Z, Lu X, Xu Q, Zhou Z (2018) Electrodeposition of nano-nickel in deep eutectic solvents for hydrogen evolution reaction in alkaline solution. *Int J Hydrogen Energy* 43:15673–15686. <https://doi.org/10.1016/J.IJHYDENE.2018.06.188>
 47. Wei XW, Zhou XM, Wu KL, Chen Y (2011) 3-D flower-like NiCo alloy nano/microstructures grown by a surfactant-assisted solvothermal process. *CrystEngComm* 13:1328–1332. <https://doi.org/10.1039/C0CE00468E>
 48. Rafique MY, Pan L, Khan WS, Iqbal MZ, Qiu H, Farooq MH, Ellahi M, Guo Z (2013) Controlled synthesis, phase formation, growth mechanism, and magnetic properties of 3-D CoNi alloy microstructures composed of nanorods. *CrystEngComm* 15:5314–5325. <https://doi.org/10.1039/C3CE40385H>
 49. Juang RS, Lin LC (2001) Electrochemical treatment of copper from aqueous citrate solutions using a cation-selective membrane. *Sep Purif Technol* 22–23:627–635. [https://doi.org/10.1016/S1383-5866\(00\)00168-4](https://doi.org/10.1016/S1383-5866(00)00168-4)
 50. Guo L, Searson PC (2010) On the influence of the nucleation overpotential on island growth in electrodeposition. *Electrochim Acta* 55:4086–4091. <https://doi.org/10.1016/J.ELECTACTA.2010.02.038>
 51. Wang S, Guo X, Yang H, Dai J, Zhu R, Gong J, Peng L, Ding W (2014) Electrodeposition mechanism and characterization of Ni–Cu alloy coatings from a eutectic-based ionic liquid. *Appl Surf Sci* 288:530–536. <https://doi.org/10.1016/J.APSUSC.2013.10.065>
 52. Pradhan D, Reddy RG (2012) Dendrite-free aluminum electrodeposition from AlCl₃–1-ethyl-3-methyl-imidazolium chloride ionic liquid electrolytes, *Metallurgical and Materials Transactions B: Process Metallurgy and Materials Processing*. Science 43:519–531. <https://doi.org/10.1007/S11663-011-9623-1>
 53. Gómez E, Cojocar P, Magagnin L, Valles E (2011) Electrodeposition of Co, Sm and SmCo from a deep eutectic solvent. *J Electroanal Chem* 658:18–24. <https://doi.org/10.1016/J.JELECHEM.2011.04.015>
 54. Gao MY, Yang C, Zhang QB, Yu YW, Hua YX, Li Y, Dong P (2016) Electrochemical fabrication of porous Ni–Cu alloy nanosheets with high catalytic activity for hydrogen evolution. *Electrochim Acta* 215:609–616. <https://doi.org/10.1016/J.ELECTACTA.2016.08.145>
 55. Yu C, Lu J, Luo L, Xu F, Shen PK, Tsiakaras P, Yin S (2019) Bifunctional catalysts for overall water splitting: CoNi oxyhydroxide nanosheets electrodeposited on titanium sheets. *Electrochim Acta* 301:449–457. <https://doi.org/10.1016/j.electacta.2019.01.149>
 56. Sivanantham A, Ganesan P, Shanmugam S (2016) Hierarchical NiCo₂S₄ nanowire arrays supported on Ni foam: an efficient and durable bifunctional electrocatalyst for oxygen and hydrogen evolution reactions. *Adv Func Mater* 26:4661–4672. <https://doi.org/10.1002/adfm.201600566>
 57. Cao Y, Liu H, Bo X, Wang F (2015) Highly active porous nickel-film electrode via polystyrene microsphere template-assisted composite electrodeposition for hydrogen-evolution reaction in alkaline medium, *Science China. Chemistry* 58:501–507. <https://doi.org/10.1007/s11426-014-5175-y>
 58. Abbas SA, Kim SH, Iqbal MI, Muhammad S, Yoon WS, Jung KD (2018) Synergistic effect of nano-Pt and Ni spine for HER in alkaline solution: hydrogen spillover from nano-Pt to

- Ni spine. *Scientific Rep* 8:1(8)1–9. <https://doi.org/10.1038/s41598-018-21396-9>
59. Jin D, Yu A, Lee Y, Kim MH, Lee C (2020) NixRh1-xOy composite nanofibres as highly efficient and robust oxygen evolution electrocatalysts. *J Alloy Compd* 836:155309. <https://doi.org/10.1016/j.jallcom.2020.155309>
60. Ghanem MA, Arunachalam P, Almayouf A, Weller MT (2016) Efficient bi-functional electrocatalysts of strontium iron oxyhalides for oxygen evolution and reduction reactions in alkaline media. *J Electrochem Soc* 163:H450–H458. <https://doi.org/10.1149/2.1171606JES/XML>
61. Wang P, Pu Z, Li Y, Wu L, Tu Z, Jiang M, Kou Z, Amiin IS, Mu S (2017) Iron-doped nickel phosphide nanosheet arrays: an efficient bifunctional electrocatalyst for water splitting. *ACS Appl Mater Interfaces* 9:26001–26007. <https://doi.org/10.1021/acsami.7b06305>
62. Ren JT, Yuan GG, Weng CC, Chen L, Yuan ZY (2018) Uniquely integrated Fe-doped Ni(OH)₂ nanosheets for highly efficient oxygen and hydrogen evolution reactions. *Nanoscale* 10:10620–10628. <https://doi.org/10.1039/c8nr01655k>
63. Yang W, Zeng J, Hua Y, Xu C, Siwal SS, Zhang Q (2019) Defect engineering of cobalt microspheres by S doping and electrochemical oxidation as efficient bifunctional and durable electrocatalysts for water splitting at high current densities. *J Power Sources* 436:226887. <https://doi.org/10.1016/J.JPOWSOUR.2019.226887>

Publisher's Note Springer Nature remains neutral with regard to jurisdictional claims in published maps and institutional affiliations.